Original scientific paper UDK: 539.3:534.2:004.942
https://doi.org/10.32762/zr.28.1.12

VIBRATION ANALYSIS OF A 2D MICROPOLAR CONTINUUM USING FINITE ELEMENTS WITH ENHANCED FIXED-POLE INTERPOLATION

VIBRACIJSKA ANALIZA 2D MIKROPOLARNOG KONTINUUMA METODOM KONAČNIH ELEMENATA S POBOLJŠANOM FIXED-POLE INTERPOLACIJOM

Laura Grbac*, Gordan Jelenić*

Abstract

In this paper, newly developed quadrilateral finite elements of arbitrary order are presented for the linear vibration analysis of a 2D micropolar continuum. For the displacement field interpolation, two types of interpolation functions based on the fixed-pole concept are considered: the original and the enhanced (linked) interpolation. The developed finite elements with 4 and 9 nodes were subsequently employed to discretise several geometrical domains. Their convergence curves for the first two natural frequencies of the selected numerical examples are critically assessed against the results obtained using standard Lagrange interpolation.

Key words: *micropolar continuum, FEM, fixed-pole approach, vibrational analysis.*

Sažetak

U ovom radu predstavljeni su novorazvijeni četverokutni konačni elementi proizvoljnog reda za linearnu vibracijsku analizu 2D mikropolarnog kontinuuma, pri čemu se za interpolaciju polja pomaka razmatraju dvije vrste funkcija temeljenih na konceptu nepomičnog pola: originalna i poboljšana (vezana) interpolacija. Razvijeni elementi s 4 i 9 čvorova korišteni su za diskretizaciju nekoliko sustava. Njihove konvergencijske krivulje za prve 2 prirodne frekvencije odabranih primjera kritički se uspoređuju s rezultatima dobivenim Lagrangeovim elementima.

Ključne riječi: *mikropolarni konitnuum, MKE, fixed-pole koncept, vibracijska analiza.*

* Sveučilište u Rijeci, Građevinski fakultet, Radmile Matejčić 3, 51000 Rijeka
E-mail: {laura.grbac, gordan.jelenic}@gradri.uniri.hr

Rad zaprimljen: 8.7.2025. Rad prihvaćen: 23.10.2025.

1. Introduction

The classical (Cauchy) theory of elasticity provides a sufficiently accurate description of the mechanical behaviour of homogeneous materials; however, numerous experimental studies have demonstrated that its simplified assumptions are inadequate for describing materials with a more pronounced (micro)structure such as e.g. foams [1]. By neglecting the influence of microstructure, the classical theory also fails to capture the so-called *size-effect*, a phenomenon observed in smaller specimens, which are stiffer than larger ones made of the same material under bending or torsion [2]. Further deviations from classical predictions have been noted in dynamic problems involving high frequencies and short wavelengths, where the microstructure affects the material response [3].

For these reasons, various generalised continuum theories have been developed, among which is the micropolar (Cosserat) theory of elasticity [4], considered in this paper. In this theory, an additional couple-stress vector occurs, resulting in generally non-symmetric stress and couple-stress tensors [4], [5], and thus there also exists an additional angular strain tensor (curvature), which is defined as the gradient of the microrotation – an additional kinematic field that describes the orientation of each material point and is completely independent of the skew-symmetric part of the displacement gradient (macrorotation) [6]. If we consider a linear-elastic, isotropic, centrosymmetric micropolar material, the relationship between the stress and couple-stress tensors on the one hand and the strain and curvature tensors on the other is described by two fourth-order constitutive tensors comprising six independent material parameters in total [7]. Reliable experimental identification methods are still lacking, which constrains broader application of the micropolar theory in engineering practice.

Therefore, the desired aim of this research is to develop and present new reliable finite elements based on micropolar theory, intended to serve both as a simulation tool directly applicable to engineering problems, and as a reliable modelling tool in virtual experimental setups to determine material parameters by inverse analysis. This contributes to the further advancement and practical implementation of Cosserat theory.

In order to develop a new displacement-based finite element for the linear analysis of a two-dimensional micropolar continuum, the application of the so-called *fixed-pole* interpolation is considered in this paper. The interpolation is inspired by the *fixed-pole* concept, which was first introduced by Bottasso and Borri in [8], where it was applied in the dynamic analysis of geometrically nonlinear 3D beams and proved to be highly effective. This approach reformulates the stress and couple-stress

resultants with respect to a unique fixed reference point, and introduces a unified kinematic field **ρ**, combining displacements and rotations.

In [9], we investigated the application of fixed-pole interpolation in the analysis of the Timoshenko beam (which is, in fact, a 1D linear micropolar continuum), where it was shown that applying the linearised form of fixed-pole interpolation ultimately yields a stiffness matrix identical to that obtained using standard Lagrange interpolation. To improve the original fixed-pole interpolation, an extensive analysis and comparison with some standard and novel interpolations were carried out in [10]. This modification emerged directly from a comparison with the linked interpolation, which is known to provide exact solutions for the Timoshenko beam subjected to arbitrary polynomial loading with a sufficient finite number of nodal points [11]. In the vibration analysis of a Timoshenko beam, it has also been shown that the ordinary fixed-pole interpolation has a favourable effect [9].

Motivated by the beneficial properties of the enhanced fixed-pole interpolation observed in the static and vibrational analysis of the 3D micropolar continuum [10], as well as by the beneficial effects of its original formulation in the vibration analysis of the Timoshenko beam [9], this paper proceeds to analyse the application of both types of fixed-pole interpolation in vibration analysis of the planar micropolar continuum. In the 2D micropolar analysis, the family of linked interpolations has previously been applied only in static problems [12], while this study extends its use to vibration analysis through a set of several existing and new numerical examples.

2. Analytical model of a linear micropolar continuum

The governing equations, including the equations of motion, kinematic and constitutive equations, are briefly outlined in the following subsections (for more detail, see e.g. [6], [7], [12], [13]).

2.1 Equations of motion

The first set of equations of motion for the micropolar continuum can be derived by applying the law of conservation of linear momentum, where the divergence theorem is applied, while the second set can be analogously derived from the law of conservation of angular momentum. Using the Einstein convention on repetitive indices, the equations of motion of a micropolar (Cosserat) continuum in linear analysis, with density ρ and microinertia coefficient j which depends on the internal structure of material, in a rectangular spatial system with co-ordinates x_1, x_2 and x_3 can be therefore written as [3]

$$\sigma_{ij,j} + p_{vi} = \rho\ddot{u}_i, \qquad \mu_{ij,j} - \varepsilon_{ijk}\sigma_{jk} + m_{vi} = \rho j\ddot{\phi}_i, \tag{1}$$

where stress tensor **σ** and the couple stress-tensor **μ** are, in general, non-symmetric, and ε_{ijk} is the permutation tensor (Levi-Civita symbol) with $\varepsilon_{123} = \varepsilon_{231} = \varepsilon_{312} = 1, \quad \varepsilon_{132} = \varepsilon_{321} = \varepsilon_{213} = -1$ with all other components equal to zero. The Kronecker delta symbol δ_{ij} is defined as $\delta_{ij} = 1$, if $i = j$, otherwise $\delta_{ij} = 0$. The first index in σ and μ denotes the direction of a stress or couple-stress components, while the second index represents the direction of the surface normal, and the comma in $\sigma_{ij,j}$ and $\mu_{ij,j}$ denotes differentiation with respect to the spatial co-ordinate x_j. The displacement and microrotation are labelled as u_i and ϕ_i, respectively, and, when accompanied by a superimposed double dot ($\ddot{\bullet}$), they represent the second derivative with respect to time, i.e., acceleration. The terms p_{vi} and m_{vi} denote the distributed volume force and moment. Since the surface is massless, the natural boundary conditions remain the same as in the static analysis (derived in detail in [12]), and they are valid at any point of the surface with prescribed loading as

$$\sigma_{ij}n_j = p_{si} \qquad \text{and} \qquad \mu_{ij}n_j = m_{si} \tag{2}$$

where n_i are components of the outward unit normal to the considered surface loaded by force loading p_{si} or moment loading m_{si}. On the remaining part of the boundary, we assign the kinematic boundary conditions.

2.2 Kinematic equations in linear analysis

When the influence of the microstructure of the material is considered, the number of degrees of freedom increases. In the micropolar continuum theory, the difference between the initial and deformed state of the body is described not only by the displacement field $\boldsymbol{u}(x_1, x_2, x_3)$, but also by the additional microrotation field $\boldsymbol{\phi}(x_1, x_2, x_3)$. The microrotation is completely independent of the displacement field as well as its derivatives [4]. The components of the non-symmetric micropolar strain tensor **ϵ** are related to those fields via

$$\epsilon_{ij} = u_{i,j} + \varepsilon_{ijk}\phi_k\,, \tag{3}$$

where we can observe that the normal micropolar strains are equal to those in the classical continuum theory, while the influence of the microrotation is present only in shear strains $\epsilon_{ij}, i, j = 1,2,3, i \neq j$. Due to the existence of an independent microrotation field **ϕ**, there also exists a corresponding change of microrotation, i.e. a curvature (angular strain) tensor **κ**, that is also non-symmetric, with components

$$\kappa_{ij} = \phi_{i,j}. \tag{4}$$

2.3 Constitutive equations

If we consider a linear elastic, isotropic, centrosymmetric micropolar material, the relations between the stresses and couple-stresses with the strains and curvatures are given by [7]

$$\sigma_{ij} = \lambda\epsilon_{kk}\delta_{ij} + (\mu + \nu)\epsilon_{ij} + (\mu - \nu)\epsilon_{ji}, \tag{5}$$

$$\mu_{ij} = \alpha\kappa_{kk}\delta_{ij} + (\beta + \gamma)\kappa_{ij} + (\beta - \gamma)\kappa_{ji}, \tag{6}$$

where the Lamé elastic constants λ and μ are known from the classical theory, while ν, α, β and γ are additional micropolar parameters. To ensure the physical meaning and stability of the material model, the following limits on these values are [14]

$$3\lambda + 2\mu > 0, \quad \mu > 0, \quad \nu > 0, \quad 3\alpha + 2\beta > 0, \quad \beta > 0, \quad \gamma > 0. \tag{7}$$

These elastic constants are related to a set of engineering parameters in the following way [15]

$$\lambda = \frac{2nG}{1-2n},\ \mu = G,\ \nu = \frac{GN^2}{1-N^2},\ \alpha = \frac{2Gl_t^2(1-\Psi)}{\Psi},\ \beta = Gl_t^2,\ \gamma = G\left(4l_b^2 - l_t^2\right), \tag{8}$$

where $G = \frac{E}{2(1+n)}$ is the shear modulus, $n \in \langle -1, 0.5\rangle$ is Poisson's ratio, E is Young's modulus, all of which are well known from classical theory; $N \in \langle 0, 1\rangle$ is a dimensionless coupling number, which is a measure of the degree of coupling between the microrotation and the macrorotation vector (skew-symmetric components of the displacement gradient) and parameter $\Psi \in \left\langle 0, \frac{3}{2}\right\rangle$ is a dimensionless polar ratio of rotational sensitivity that has a similar effect in torsion as Poisson's ratio has in axial deformation. The characteristic lengths for bending l_b and for torsion l_t are the parameters, which represent a measure of the respective stiffening due to the microstructure of the material, and they introduce the *size-effect* phenomenon into consideration [16]. The influence of the microstructure of the material on its macroscopic behaviour becomes relatively minor when the values of the characteristic lengths are sufficiently small compared to representative dimensions of the observed specimen.

2.4 Plane strain formulation

In the two-dimensional case there are only three degrees of freedom, i.e. two displacements $\boldsymbol{u} = [u_1 \quad u_2 \quad 0]^{\mathrm{T}}$, and one in-plane (drilling), microrotation $\boldsymbol{\phi} = [0 \quad 0 \quad \phi_3]^{\mathrm{T}}$. Hence, the kinematic equations in their matrix form are reduced as follows

$$\underbrace{\begin{Bmatrix}\epsilon_{11}\\ \epsilon_{12}\\ \epsilon_{21}\\ \epsilon_{22}\end{Bmatrix}}_{\boldsymbol{\epsilon}} = \underbrace{\begin{bmatrix}\frac{\partial}{\partial x_1} & 0\\ \frac{\partial}{\partial x_2} & 0\\ 0 & \frac{\partial}{\partial x_1}\\ 0 & \frac{\partial}{\partial x_2}\end{bmatrix}}_{\boldsymbol{D_u^T}} \underbrace{\begin{Bmatrix}u_1\\ u_2\end{Bmatrix}}_{\boldsymbol{u}} + \underbrace{\begin{Bmatrix}0\\ 1\\ -1\\ 0\end{Bmatrix}}_{\boldsymbol{I_\phi}} \phi_3 \Leftrightarrow \boldsymbol{\epsilon} = \boldsymbol{D_u^T u} + \boldsymbol{I_\phi}\phi_3, \tag{9}$$

and

$$\underbrace{\begin{Bmatrix}\kappa_{31}\\ \kappa_{32}\end{Bmatrix}}_{\boldsymbol{\kappa}} = \underbrace{\begin{Bmatrix}\frac{\partial}{\partial x_1}\\ \frac{\partial}{\partial x_2}\end{Bmatrix}}_{\boldsymbol{D_\phi^T}} \phi_3 \Leftrightarrow \boldsymbol{\kappa} = \boldsymbol{D_\phi}^{\mathrm{T}}\phi_3 \tag{10}$$

In the plane strain state it is assumed that the strain components involving the x_3 direction are equal to zero, that is $\epsilon_{33} = \epsilon_{13} = \epsilon_{23} = \epsilon_{31} = \epsilon_{32} = 0$, while all curvature components associated with microrotations about the x_1 and x_2 axes, as well as all derivatives with respect to the out-of-plane coordinate, also vanish, i.e., $\kappa_{11} = \kappa_{12} = \kappa_{21} = \kappa_{22} = \kappa_{23} = \kappa_{13} = \kappa_{33} = 0$. This yields the reduced constitutive equations expressed in terms of engineering material parameters for the plane-strain state as follows

$$\begin{Bmatrix}\sigma_{11}\\ \sigma_{12}\\ \sigma_{21}\\ \sigma_{22}\end{Bmatrix} = \frac{E}{1+n}\begin{bmatrix}\frac{1-n}{1-2n} & 0 & 0 & \frac{n}{1-2n}\\ 0 & \frac{1}{2(1-N^2)} & \frac{1-2N^2}{2(1-N^2)} & 0\\ 0 & \frac{1-2N^2}{2(1-N^2)} & \frac{1}{2(1-N^2)} & 0\\ \frac{n}{1-2n} & 0 & 0 & \frac{1-n}{1-2n}\end{bmatrix}\begin{Bmatrix}\epsilon_{11}\\ \epsilon_{12}\\ \epsilon_{21}\\ \epsilon_{22}\end{Bmatrix} \Leftrightarrow \boldsymbol{\sigma} = \boldsymbol{C_1}\boldsymbol{\epsilon} \tag{11}$$

$$\begin{Bmatrix}\mu_{31}\\ \mu_{32}\end{Bmatrix} = \frac{2El_b^2}{1+n}\begin{bmatrix}1 & 0\\ 0 & 1\end{bmatrix}\begin{Bmatrix}\kappa_{31}\\ \kappa_{32}\end{Bmatrix} \Leftrightarrow \boldsymbol{\mu} = \boldsymbol{C_2}\boldsymbol{\kappa} \tag{12}$$

where $\boldsymbol{C_1}$ and $\boldsymbol{C_2}$are constitutive matrices. The elastic constant α, as well as the engineering parameters Ψ and l_t do not take place in 2D formulation. The first set of constitutive equations for the plane stress condition can be found in [7], while the second set remains the same as for the plane strain. In this paper, the analysis is restricted to the plane strain case since the available benchmark examples from the literature are presented only for this condition.

3. Finite element analysis of a 2D micropolar continuum

To construct a numerical solution procedure for a boundary value problem, the strong (differential) form is replaced by an integral (weak) form derived from D'Alembert's principle, which extends the virtual work principle to dynamic problems in a 2D micropolar continuum with a constant thickness t and 2D domain S with its boundary curve s, as follows

$$\begin{aligned}\int_S t(\overline{\boldsymbol{\epsilon}}^T \boldsymbol{C}_1 \boldsymbol{\epsilon} + \overline{\boldsymbol{\kappa}}^T \boldsymbol{C}_2 \boldsymbol{\kappa}) dS - \int_S t(\overline{\boldsymbol{u}}^T (\boldsymbol{p}_v - \rho \ddot{\boldsymbol{u}}) + \overline{\boldsymbol{\phi}}^T (\boldsymbol{m}_v - \rho j \ddot{\boldsymbol{\phi}})) dS \\ - \oint_s t(\overline{\boldsymbol{u}}^T \boldsymbol{p}_s + \overline{\boldsymbol{\phi}}^T \boldsymbol{m}_s)\, ds = 0,\end{aligned} \tag{13}$$

based on which a set of algebraic equations of motion will be obtained according to the finite element method after the introduction of interpolation functions for the real and virtual kinematic fields, the latter denoted by an overbar. After introducing kinematic equations (9) and (10), the kinematic fields have to be approximated using a chosen interpolation in order to obtain the numerical solution of a problem.

3.1 Enhanced fixed-pole interpolation

Here, we introduce the *enhanced fixed-pole interpolation* (*EFP*) interpolation for approximating the displacement field $\boldsymbol{u}$ as [10]

$$\boldsymbol{u} = \sum_{i=1}^{m} N_i \left(\boldsymbol{\rho}_i - \frac{1}{k} \hat{\boldsymbol{r}} \boldsymbol{\phi} \right), \tag{14}$$

for an arbitrary number of finite element nodes $m = k^d$, where k represents the number of nodes along the finite element's side, and d is the spatial dimension of finite element, i.e. $d = 1, 2, 3$ for 1D, 2D and 3D respectively. Here, N_i are Lagrange polynomials of order $m-1$, for $i = 1, \ldots, m$, while $\boldsymbol{r}^h = \sum_{i=1}^{m} N_i \boldsymbol{r}_i{}^e$ denotes the interpolated initial position vector, where $\boldsymbol{r}_i{}^e = \langle r_{x1i}{}^e \quad r_{x2i}{}^e \rangle^T$ is a vector of the nodal coordinates of the i^{th} node. The nonstandard kinematic field is defined as $\boldsymbol{\rho} = \mathbf{u} + \hat{\boldsymbol{r}} \boldsymbol{\phi}$, where the operator $\hat{\bullet}$ represents the antisymmetric matrix equivalent to the vector cross product, such that $\boldsymbol{r} \times \boldsymbol{\phi} = \hat{\boldsymbol{r}} \boldsymbol{\phi}$. The rotation field is interpolated using standard Lagrange interpolation: $\boldsymbol{\phi} = \sum_{i=1}^{m} N_i \boldsymbol{\phi}_i$. This formulation was originally presented in [17], where it was applied to the numerical analysis of a three-dimensional micropolar continuum, and here is reduced for the two-dimensional case.

For approximation of the displacement field $\boldsymbol{u}^h = \boldsymbol{N}_u \boldsymbol{p}^e$ and the virtual displacement field $\overline{\boldsymbol{u}}^h = \boldsymbol{N}_u \overline{\boldsymbol{p}}^e$, the same enhanced fixed-pole interpolation is used (Bubnov-Galerkin approach), where superscript h denotes the finite element approximation, and superscript e refers to the element to which the interpolation is applied. The matrix of interpolation functions is

$$\boldsymbol{N}_u = [\boldsymbol{N}_1 \quad \boldsymbol{0} \quad \dots \quad \boldsymbol{N}_m \quad \boldsymbol{0}] - \frac{1}{k}\begin{bmatrix} 0 & 1 \\ -1 & 0 \end{bmatrix}\boldsymbol{r}[\boldsymbol{0^T} \quad N_1 \quad \dots \quad \boldsymbol{0^T} \quad N_m], \tag{15}$$

with the 2D position vector $\boldsymbol{r} = \sum_{i=1}^{m} N_i \boldsymbol{r}_i$ and zero vector $\boldsymbol{0^T} = [0 \quad 0]$. The sub-matrices $\boldsymbol{N}_i$ of the Lagrange polynomials of order $m-1$ are given as $\boldsymbol{N}_i = N_i \boldsymbol{I}$ for $i = 1, \dots, m$, where $m = k^2$ stands for the total number of nodes of each 2D finite element. The microrotation and virtual microrotation fields have been interpolated by standard Lagrange polynomials as $\boldsymbol{\phi}^h = \boldsymbol{N}_\phi \boldsymbol{p}^e$ and $\overline{\boldsymbol{\phi}}^h = \boldsymbol{N}_\phi \overline{\boldsymbol{p}}^e$ with $\boldsymbol{N}_\phi = [\boldsymbol{0^T} \quad N_1 \quad \dots \quad \boldsymbol{0^T} \quad N_m]$. By introducing the chosen shape functions for the unknown fields

$$\boldsymbol{p}^e = \langle \boldsymbol{p}_1^T \quad \boldsymbol{p}_2^T \quad \dots \quad \boldsymbol{p}_m^T \rangle^{eT}, \quad \overline{\boldsymbol{p}}^e = \langle \overline{\boldsymbol{p}}_1^T \quad \overline{\boldsymbol{p}}_2^T \quad \dots \quad \overline{\boldsymbol{p}}_m^T \rangle^{eT}, \tag{16}$$

with non-standard degrees of freedom

$$\boldsymbol{p}_i^T = \langle \rho_{1i} \quad \rho_{2i} \quad \phi_{3i} \rangle^T, \quad \overline{\boldsymbol{p}}_i^T = \langle \overline{\rho}_{1i} \quad \overline{\rho}_{2i} \quad \overline{\phi}_{3i} \rangle^T, \text{ for } i = 1, \dots, m, \tag{17}$$

the equation of motion of a 2D micropolar finite element mesh with arbitrary chosen number of nodes m can thus be obtained as

$$\begin{aligned} \mathop{\mathbb{A}}_{e=1}^{n_{el}} \overline{\boldsymbol{p}}^{eT} \Big[\int_S \; t \Big[\Big(\boldsymbol{B}_\rho^T - \frac{1}{k}\boldsymbol{B}_R^T + \Big(\frac{k-1}{k}\Big)\boldsymbol{B}_{I\phi}^T \Big) \boldsymbol{C}_1 \Big(\boldsymbol{B}_\rho - \frac{1}{k}\boldsymbol{B}_R + \Big(\frac{k-1}{k}\Big)\boldsymbol{B}_{I\phi} \Big) \\ + \big(\boldsymbol{N}_\phi^T \boldsymbol{D}_\phi{}^T \big) \boldsymbol{C}_2 \big(\boldsymbol{D}_\phi \boldsymbol{N}_\phi \big) \Big] dS \boldsymbol{p}^e + \int_S t \begin{bmatrix} \rho \boldsymbol{N}_u^T \boldsymbol{N}_u & \boldsymbol{0} \\ \boldsymbol{0^T} & \boldsymbol{N}_\phi^T \rho j \boldsymbol{N}_\phi \end{bmatrix} dS \ddot{\boldsymbol{p}}^e - \\ \int_S t \left(\begin{bmatrix} \boldsymbol{N}_u{}^T \\ \boldsymbol{N}_\phi{}^T \end{bmatrix}^T \begin{Bmatrix} \boldsymbol{p}_v \\ \boldsymbol{m}_v \end{Bmatrix} \right) dS - \int_S \left(\begin{bmatrix} \boldsymbol{N}_u{}^T \\ \boldsymbol{N}_\phi{}^T \end{bmatrix}^T \begin{Bmatrix} \boldsymbol{p}_s \\ \boldsymbol{m}_s \end{Bmatrix} \right) dS \Big] = 0, \end{aligned} \tag{18}$$

$$\mathop{\mathbb{A}}_{e=1}^{n_{el}} \overline{\boldsymbol{p}}^{eT} (\boldsymbol{K}^e \boldsymbol{p}^e + \boldsymbol{M}^e \ddot{\boldsymbol{p}}^e - \boldsymbol{f}^e) = 0. \tag{19}$$

In equation (19), $\boldsymbol{K}^e$, $\boldsymbol{M}^e$ and $\boldsymbol{f}^e$ represent the element stiffness and mass matrix and external force vector of an element e, for $e = 1, \dots, n_{el}$, where n_{el} is the total number of elements in a mesh, t stands for the thickness of the finite element and $\mathbb{A}$ is the finite-element assembly operator.

The $\boldsymbol{B}$ matrices of mutual dependence of the strains in the element with unknown nodal degrees of freedom in (18) are $\boldsymbol{B}_\rho = \begin{bmatrix} \boldsymbol{B}_{\rho 1} & \boldsymbol{0} \\ \boldsymbol{0} & \boldsymbol{0} \end{bmatrix} \dots \begin{bmatrix} \boldsymbol{B}_{\rho m} & \boldsymbol{0} \\ \boldsymbol{0} & \boldsymbol{0} \end{bmatrix}$, $\boldsymbol{B}_R = [\boldsymbol{0^T} \quad \boldsymbol{0^T} \quad \boldsymbol{B}_{R1} \quad \dots \quad \boldsymbol{0^T} \quad \boldsymbol{0^T} \quad \boldsymbol{B}_{Rm}]$, $\boldsymbol{B}_{I\phi} = \begin{bmatrix} \boldsymbol{0^T} & \boldsymbol{0^T} & \boldsymbol{B}_{I\phi 1} & \dots & \boldsymbol{0^T} & \boldsymbol{0^T} & \boldsymbol{B}_{I\phi m} \end{bmatrix}$, while the sub-matrices in $\boldsymbol{B}_\rho$, $\boldsymbol{B}_R$ and $\boldsymbol{B}_{I\phi}$ are

$$\boldsymbol{B}_{\rho i} = \begin{bmatrix} \frac{\partial N_i}{\partial x_1} & 0 \\ \frac{\partial N_i}{\partial x_2} & 0 \\ 0 & \frac{\partial N_i}{\partial x_1} \\ 0 & \frac{\partial N_i}{\partial x_2} \end{bmatrix}, \quad \boldsymbol{B}_{Ri} = \begin{bmatrix} r_{x2i}\frac{\partial N_i}{\partial x_1} \\ r_{x2i}\frac{\partial N_i}{\partial x_2} \\ -r_{x1i}\frac{\partial N_i}{\partial x_1} \\ -r_{x1i}\frac{\partial N_i}{\partial x_2} \end{bmatrix}, \quad \boldsymbol{B}_{I\phi i} = \begin{bmatrix} 0 \\ N_i \\ -N_i \\ 0 \end{bmatrix}. \tag{20}$$

It is also important to note that the external loads should be determined according to the chosen interpolation functions when satisfying the finite element equilibrium equation. In other words, the external moments should be defined with respect to the fixed pole exactly as it has been shown in (18).

3.2 Quadrilateral micropolar FE with four and nine nodes

For discretisation of the 2D micropolar continuum, quadrilateral finite elements with 4 and 9 nodes with three degrees of freedom per node have been chosen, where the proposed enhanced fixed-pole interpolation is used to interpolate the displacement field and Lagrange interpolation for the rotational field. The mapping between the natural and global coordinate system is defined as $\mathbf{x}^h = \sum_{i=1}^{m} N_i(\xi,\eta)\mathbf{x}_i^e$, where $\mathbf{x}_i^e = \langle x_{1i}^e \quad x_{2i}^e \rangle^T$ and x_{1i}^e, x_{2i}^e are the i^{th} node coordinates of an element. The Lagrange polynomials for the quadrilateral element with four nodes $m = 4$ ($Q4$) are

$$N_i(\xi,\eta) = \frac{1}{4}[(1+\xi_i\xi)(1+\eta_i\eta)], \text{ for } i = 1,\dots 4, \tag{21}$$

where $\xi_i = \pm 1, \eta_i = \pm 1$ are assigned according to the position of the nodes such that $(\xi_i,\eta_i) = (-1,-1),\ (1,-1),\ (1,1),\ (-1,1)$ for $i = 1,\dots,4$. Lagrange polynomials for the quadrilateral element with nine nodes ($Q9$) are given as [18]

- For corner nodes:

$$N_i(\xi,\eta) = \frac{1}{4}\xi\eta(\xi+\xi_i)(\eta+\eta_i), \text{ for } i = 1,\dots 4, \text{ where } \xi_i = \pm 1, \eta_i = \pm 1 \tag{22}$$

- Mid-side nodes:

$$N_{i+4}(\xi,\eta) = \frac{1}{2}\eta(1-\xi^2)(\eta+\eta_{i+4}), \text{ for } i = 1,3,$$

$$N_{i+4}(\xi,\eta) = \frac{1}{2}\xi(\xi+\xi_{i+4})(1-\eta^2), \text{ for } i = 2,4, \tag{23}$$

where $\xi_5 = \xi_7 = 0, \eta_5 = -1, \eta_7 = 1$, and $\xi_6 = 1, \xi_8 = -1, \eta_6 = \eta_8 = 0$.

- Middle node: $N_9 = (1-\xi^2)(1-\eta^2)$. (24)

After introducing the chosen interpolation into (18), the full numerical integration procedure has been applied (following [18]) in order to compute the element mass and stiffness matrix and the load vector. In terms of the standard degrees of freedom $\boldsymbol{p}_s^e = \langle \boldsymbol{p}_{s1}^T \quad \cdots \quad \boldsymbol{p}_{sm}^T \rangle^{eT}$, with $\boldsymbol{p}_{si}^T = \langle u_{1i} \quad u_{2i} \quad \phi_{3i} \rangle^T$ approximated weak form (19) may be written as

$$\overline{\boldsymbol{p}}_s^T(\boldsymbol{K}_s\boldsymbol{p}_s + \boldsymbol{M}_s\ddot{\boldsymbol{p}}_s - \boldsymbol{f}_s) = 0 \text{ for arbitrary } \overline{\boldsymbol{p}}_s \Rightarrow \boldsymbol{K}_s\boldsymbol{p}_s + \boldsymbol{M}_s\ddot{\boldsymbol{p}}_s = \boldsymbol{f}_s, \quad (25)$$

with $\boldsymbol{M}_s = \mathop{\mathbb{A}}_{e=1}^{n_{el}} \boldsymbol{M}_s^e$, $\boldsymbol{K}_s = \mathop{\mathbb{A}}_{e=1}^{n_{el}} \boldsymbol{K}_s^e$ and $\boldsymbol{f}_s = \mathop{\mathbb{A}}_{e=1}^{n_{el}} \boldsymbol{f}_s^e$, where $\boldsymbol{K}_s^e = \boldsymbol{R}_o^e \boldsymbol{K}^e \boldsymbol{R}_o^{eT}$ and $\boldsymbol{M}_s^e = \boldsymbol{R}_o^e \boldsymbol{M}^e \boldsymbol{R}_o^{eT}$ where $\boldsymbol{R}_o^e$ follows from (14) as

$$\boldsymbol{R}_o^e = \begin{bmatrix} \boldsymbol{I} & \boldsymbol{0} & \cdots & \boldsymbol{0} & \boldsymbol{0} \\ \left[\frac{1}{k}\begin{bmatrix} 0 & 1 \\ -1 & 0 \end{bmatrix}\boldsymbol{r}_1\right]^T & 1 & \cdots & \boldsymbol{0} & \boldsymbol{0} \\ \vdots & \vdots & \ddots & \vdots & \vdots \\ \boldsymbol{0} & \boldsymbol{0} & \cdots & \boldsymbol{I} & \boldsymbol{0} \\ \boldsymbol{0} & \boldsymbol{0} & \cdots & \left[\frac{1}{k}\begin{bmatrix} 0 & 1 \\ -1 & 0 \end{bmatrix}\boldsymbol{r}_{n_{el}}\right]^T & 1 \end{bmatrix}. \quad (26)$$

4. Numerical examples

The newly developed micropolar finite elements (*Q4EFP* and *Q9EFP*) have been implemented in *FEAP* (Finite Element Analysis Program [19]). The convergence of the proposed finite element has been evaluated by performing a set of patch tests specifically derived for micropolar finite elements (for detail, see [20], [21]). Since the proposed *EFP* formulation, ultimately results in a formulation that is identical to that presented in [21], where quadrilateral FE with the linked interpolation were used only for static analysis, the numerical results of these patch tests are identical, and therefore there is no need to present them in detail here. However, it should be emphasised that the Petrov-Galerkin approach followed in [21] is not applied here, and that the fixed-pole formulation can be generalised to higher order elements in a very elegant way. In static analysis, this family of elements has already been shown to be convergent and capable of eliminating *shear-locking*, thus achieving faster convergence towards the exact solution compared to conventional elements (as demonstrated on the benchmark example of pure bending [17], [21]). On the other hand, the application of such a finite element formulation for the dynamic analysis of a planar micropolar continuum has not yet been reported.

4.1 Vibration analysis

A free vibration analysis for the following problems has been conducted:

i. Planar cantilever beam (CF) of length $L = 3.3$ mm and height $h = 0.165$ mm,

ii. Planar beam clamped on both sides (CC) with the same properties as in (*i*),

iii. Cantilever square planar membrane with a central circular hole (CF) with edge-length $L = 3.3$ mm and radius of the hole $r = 0.33$ mm,

iv. Fully clamped circular planar membrane of radius $R = 1.65$ mm with a central circular hole $r = 0.33$ mm,

while the thickness t in all examples is taken as unity. All clamped boundaries are defined by restraining all three degrees of freedom along the entire edge — over the full side(s) for the rectangular domains and along the outer circumference for the circular domain. The material properties are as in [22]: $G = 104$ MPa, $n = 0.44$, $N^2 = 0.04$, $l_b = 0.33$ mm, $l_t = 0.62$ mm, $\Psi = 1.5$, $\rho = 2000$ kg/m^3, $j = 5 \cdot 10^{-5}$ m^2, $\rho j = 10^{-1}$ kg/m. Schematic presentations of the geometries and FE discretisations of the square and circular planar membranes with a hole are shown in Figure 1.

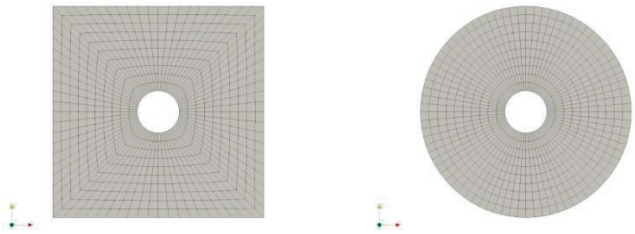

Figure 1. Schematic representation of discretisation in numerical examples (*iii* - left) and (*iv* - right) with a mesh of 10x10 elements per each quadrant

The present quadrilateral micropolar FE with four nodes *Q4EFP* and with nine nodes *Q9EFP* have been used to discretise those geometries. The coefficient *k* appearing in the enhanced fixed-pole interpolation stands for the number of nodes along the element edge, i.e. *k* = 2 for *Q4EFP* and *k* = 3 for *Q9EFP*. The numerical results have been also obtained using the original fixed-pole interpolation (*Q4OFP* and *Q9OFP* with *k* = 1) and the standard Lagrange interpolation *LI* (elements *Q4LI, Q9LI*). In the analysis of the Timoshenko beam, the application of *EFP* interpolation produces a stiffness matrix equivalent to that obtained using Lagrange interpolation with reduced numerical integration, thus eliminating *shear-locking*. In the case of continuum analysis, this equivalence no longer holds, and reduced

numerical integration can be applied to further improve the accuracy of the results. Therefore, in the numerical examples presented here, both full and reduced numerical integration are employed for the computation of the stiffness matrix in the case of lower-order elements. Figures 2 – 5 show the convergence curves for the first two natural frequencies obtained using *Q4* elements with full integration (first row), *Q4* with reduced integration (second row), and *Q9* with full integration (third row). At the higher frequencies, all three curves seem to match quite closely. The reference solutions have been computed using very dense meshes of Q9LI elements. The reference solutions for the problems (*i*) and (*iv*) coincide with the numerical results from [22], which verifies the accuracy of the model. Based on this, we analyse the problems (*ii*) and (*iii*) with different boundary conditions. The reference solutions can be found in Table 1.

Table 1. R*eference solutions for the natural frequencies (f_1 and f_2) of all four considered numerical example.*

Example	f_1 [kHz]	f_2 [kHz]
CF beam (*i*) [22]	1.59481	4.76076
CC beam (*ii*)	3.75830	6.45379
Square membrane (*iii*)	2.43085	3.96779
Circular membrane (*iv*) [22]	5.68080	7.54525

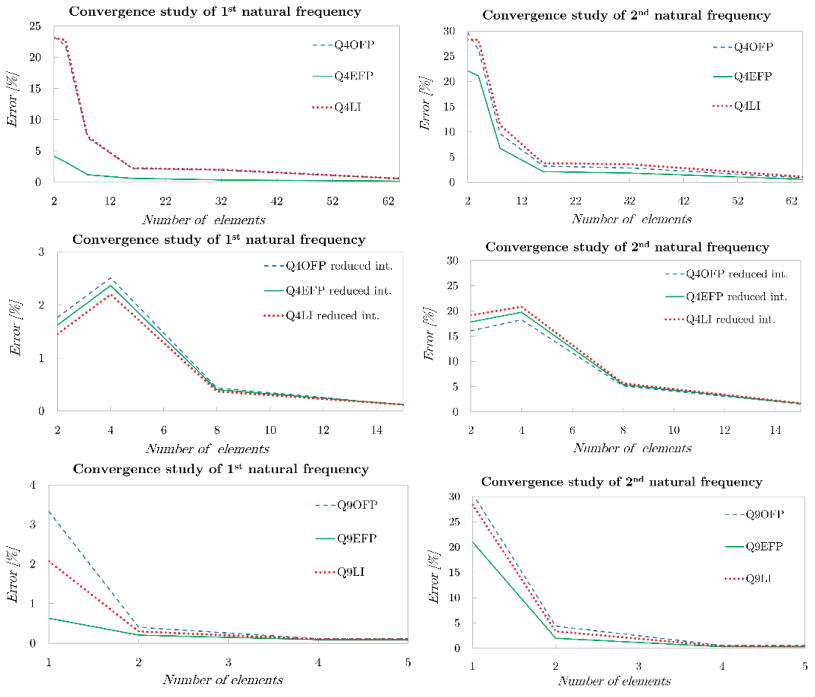

Figure 2. Convergence of the first (left) and second (right) natural frequencies of the cantilever beam (*i*)

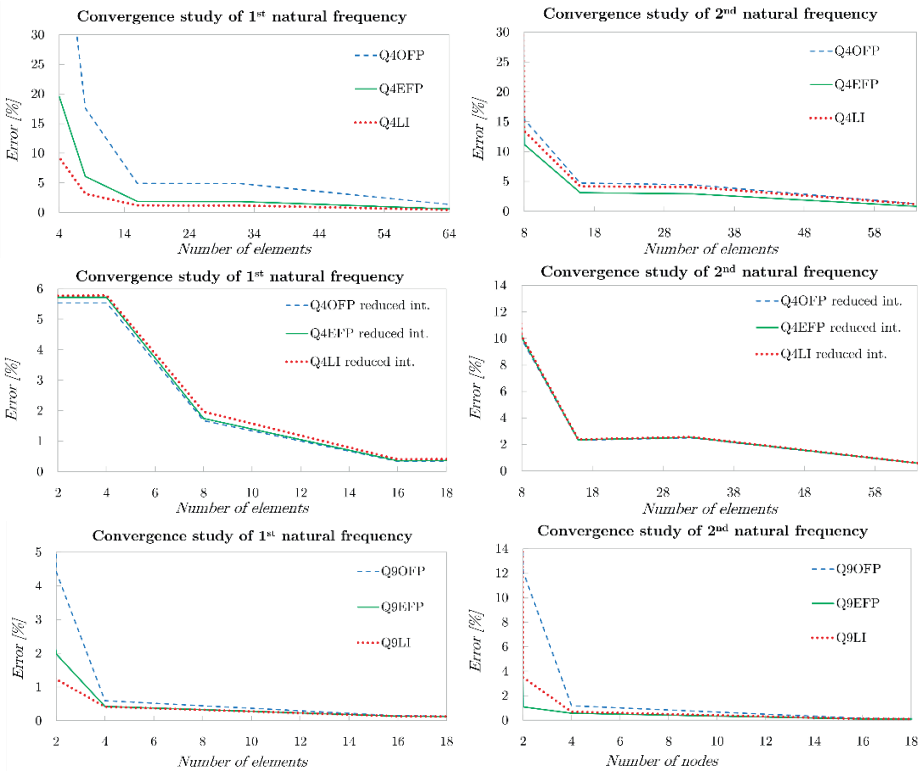

Figure 3. Convergence of the first (left) and second (right) natural frequencies for the fully clamped (*ii*)

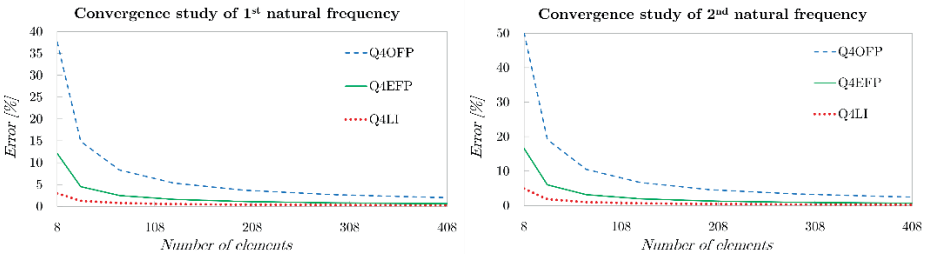

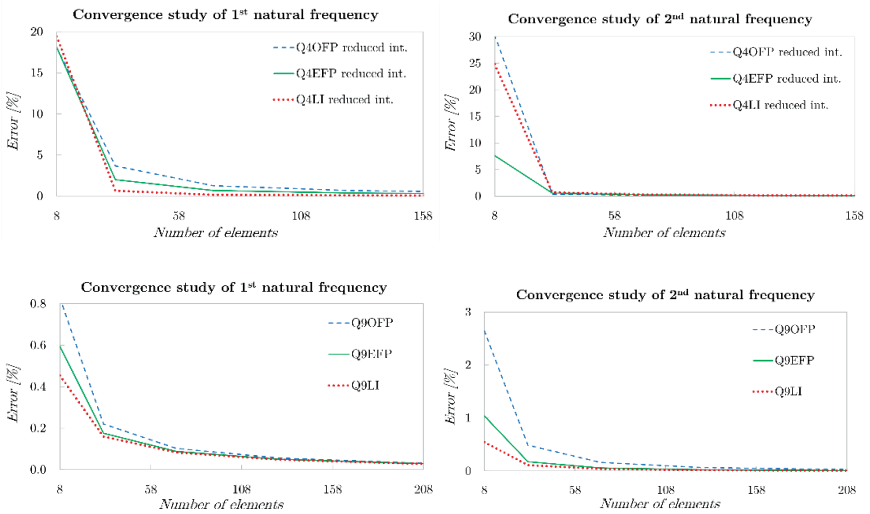

Figure 4. Convergence study of the first (left) and second (right) natural frequencies for the cantilever square planar membrane with a circular hole (*iii*)

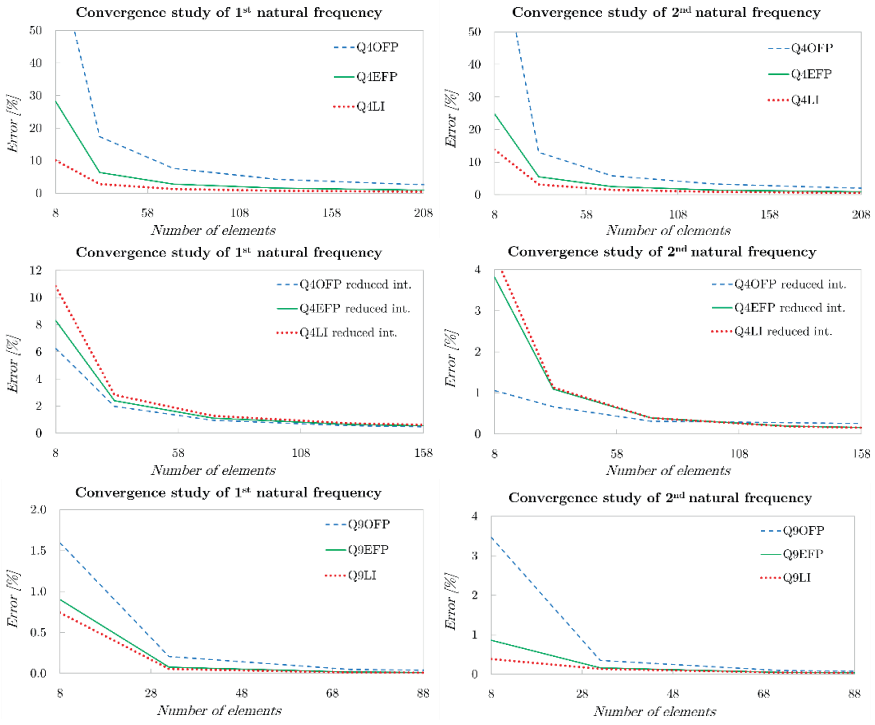

Figure 5. Convergence study of the first (left) and second (right) natural frequencies for the circular planar membrane with a circular hole (*iv*)

The convergence study of the first two natural frequencies for the planar beam (*i*), shown in Figure 2, clearly demonstrates the efficiency of the *Q4* and *Q9* elements with the *EFP* interpolation and full numerical integration, compared to the other two. However, this difference in efficiency is smaller for the planar beam clamped on both sides (*ii*), as observed in Figure 3 for the second frequency, while for the first frequency, the Lagrange elements show slightly better results. It should be emphasised that the presented numerical examples are discretised using membrane finite elements under plane-strain conditions, and that the in-plane vibrations of the model are considered. In the second example (*ii*), the additional boundary constraints on the right end further increase the overall stiffness of the system, which may favour the Lagrange elements due to their inherently stiffer formulation for coarse meshes. To further investigate the influence of model stiffness, an additional analysis of the same CC beam (ii_b) has been performed,with identical geometric and material properties except for the characteristic length, which has been reduced ten times; that is, the characteristic length is now $l_b = 0.033$ mm, giving $\frac{l_b}{h} = 0.2$. A smaller characteristic length reduces the influence of the microstructure, resulting in a softer response and lower natural frequencies. The reference solutions, obtained numerically in the same way as for the previous examples, are $f_1 = 0.81000909$ and $f_2 = 1.07559623$ [kHz]. Figure 6 shows the convergence study of the first two natural frequencies for the planar beam (ii_b) using *Q4* elements with full numerical integration, where the proposed *EFP* interpolation now demonstrates faster convergence compared to the other two approaches.

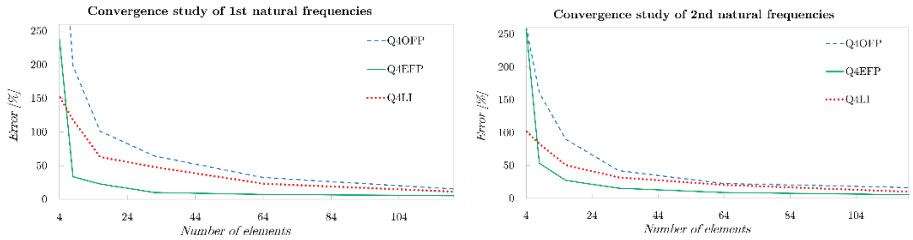

Figure 6. Convergence of the first (left) and second (right) natural frequencies for the fully clamped (ii_b)

For the cases of the square and circular planar membrane with a circular hole, we have results indicating that the Lagrange interpolation provides the most accurate description for coarse meshes, as illustrated in Figures 4 and 5. All elements, however, exhibit proper convergence with mesh refinement. To better understand this somewhat unexpected behaviour, a numerical example from reference [10] that represents a 3D square domain with a central circular hole has been considered. In that study, for

the cantilever configuration, the 3D micropolar finite elements with *EFP* interpolation clearly demonstrated higher efficiency. The main reason why the present planar analysis leads to somewhat different conclusions may lie in the plane-strain assumption adopted here, as well as in the geometric proportions of the analysed model. In the present (*iii*) case, the ratio between the side length of the square domain and the hole radius is $\frac{L}{r} = 10$, whereas in reference [10] the side length is $L = 33$ mm, and the radius is $r = 0.3L$, giving $\frac{L}{r} = 3.3$ (i.e., a larger hole and therefore a less stiff configuration). When the 3D numerical example [10] is reduced to plane-strain conditions as an additional case (iii_b), with unchanged material parameters and using *Q4* elements with full numerical integration, the reference solutions for the first two natural frequencies are $f_1 = 0.82229$ and $f_2 = 1.57183$ [kHz]. A visibly faster convergence of the *EFP* and *OFP* interpolations is obtained for the first natural frequency, while for the second frequency, the results of the *Q4LI* and *Q4EFP* elements almost coincide, as shown in Figure 7.

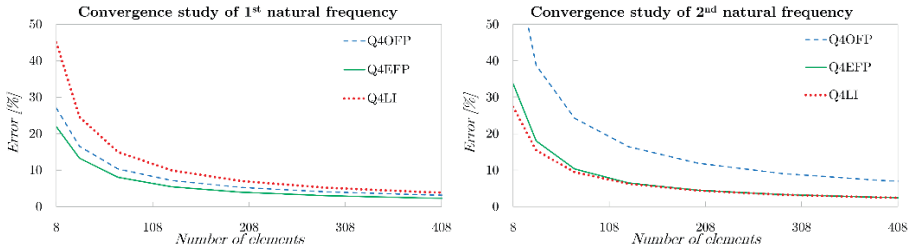

Figure 7. Convergence of the first (left) and second (right) natural frequencies for the fully clamped (iii_b)

For the mesh consisting of only eight elements, the maximum difference in error between the numerical results obtained using *Q4LI* and *Q4EFP* elements for the first two eigenfrequencies is 18.08% for case (*iv*) in the first mode, whereas the maximum difference between *Q9LI* and *Q9EFP* elements is 0.47% for the second mode of case (*iv*). It can be observed that in the case of the circular planar membrane (*iv*), the Lagrange elements provide the most accurate results on coarse meshes. In this numerical example, the membrane is fully clamped along the entire outer circular edge, which makes the system very stiff. In the future work, it would be useful to conduct additional analyses with different boundary conditions allowing more degrees of freedom.

In contrast to the conclusions drawn in the analysis of the Timoshenko beam [9], here the original fixed-pole interpolation does not improve the results. Moreover, in all cases, where the full numerical integration is

employed, it gives either the same or worse results than the Lagrange interpolation, which leads us to the conclusion that this type of interpolation should not be recommended for application in a micropolar continuum if the reduced numerical interpolation is not applied. In all numerical examples, all formulations employing reduced numerical integration provide more accurate results on coarse meshes in general. The differences between the formulations become evident in examples (*iii*) and (*iv*), for the second natural frequency, where the *EFP* and *OFP* interpolations yield the most accurate results, respectively.

5. Conclusion

In this paper, new two-dimensional micropolar finite elements of arbitrary order have been developed using the enhanced fixed-pole (*EFP*) interpolation. While it is well established that this formulation achieves faster convergence to the exact solution in linear static analysis compared to standard Lagrange elements, the vibration analysis presented here introduces several new numerical examples that reveal a more diverse behaviour. The improvement offered by the *EFP* interpolation is observed only in certain cases, whereas the Lagrange elements tend to perform slightly better for stiffer models and when full numerical integration is applied. Given the limited literature addressing the dynamic behaviour of micropolar continua, the present study contributes new benchmark results and provides a solid basis for further investigations. Future work will focus on a detailed parametric study on the influence of micropolar material parameters on the vibration response, as well as on the possibility of extending the applicability of the fixed-pole concept to problems involving large three-dimensional rotations within the micropolar continuum.

Acknowledgments. *The presented research has been financially supported by the CSF projects (HRZZ-DOK-2018-09-8806 and HRZZ-IP-2024-05-9904) as well as (uniri-mz-25-19).*

References

[1] Lakes, R. S. (2023) Experimental Evaluation of Micromorphic Elastic Constants in Foams and Lattices. ZAMP, 74 (1), str. 1–11.

[2] Drugan, W. J., Lakes, R. S. (2018) Torsion of a Cosserat Elastic Bar with Square Cross Section: Theory and Experiment. ZAMP, 69 (2).

[3] Nowacki, W. K. (1985) Theory of Asymmetric Elasticity. Warszawa: Pergamon Press.

[4] Cosserat, E., Cosserat, F. (1909) Théorie des corps déformables. Paris: Herman.

[5] Voigt, W. (1887) Theoretische Studien über die Elasticitätsverhältnisse der Krystalle. Abh. Königl. Ges. Wiss. Göttingen, 3 (34), str. 3–52.

[6] Eringen, A. C. (2012) Microcontinuum Field Theories: I. Foundations and Solids. New York: Springer Verlag.

[7] Nowacki, W. (1974) The Linear Theory of Micropolar Elasticity. Courses and lectures CISM, Udine, str. 1–43.

[8] Bottasso, C. L., Borri, M. (1998) Integrating Finite Rotations. Computational Methods in Applied Mechanics and Engineering, 164 (3–4), str. 307–331.

[9] Žiković, L., Jelenić, G. (2021) Primjena fixed-pole interpolacije u linearnoj dinamičkoj analizi Timošenkove grede. Zbornik radova 11. susreta HDM-a. Rijeka, HDM, str. 369–375.

[10] Grbac, L., Jelenić, G., Ribarić, D., Grbčić Erdelj, S. (2024) Hexahedral Finite Elements with Enhanced Fixed-Pole Interpolation for Linear Static and Vibration Analysis of 3D Micropolar Continuum. IJNME, 125 (8), str. 1-27.

[11] Jelenić, G., Papa, E. (2011) Exact Solution of 3D Timoshenko Beam Problem Using Linked Interpolation of Arbitrary Order. Arch. Appl. Mech., 81 (2), str. 171–183.

[12] Grbčić, S. (2018) Linked Interpolation and Strain Invariance in Finite-Element Modelling of Micropolar Continuum (Ph.D. thesis). University of Rijeka and Université de Technologie de Compiègne – Sorbonne Universités.

[13] Hassanpour, S., Heppler, G. R. (2015) Micropolar Elasticity Theory: a Survey of Linear Isotropic Equations, Representative Notations, and Experimental Investigations. Mathematics and Mechanics of Solids, 22 (2), str. 224–242.

[14] Gauthier, R. D., Jahsman, W. E. (1975) A Quest for Micropolar Elastic Constants. Journal of Applied Mechanics, 42 (2), str. 369–374.

[15] Lakes, R. (2016) Physical Meaning of Elastic Constants in Cosserat, Void, and Microstretch Elasticity. J. Mech. Mater. Struct., 11 (3), str. 217–229.

[16] Anderson, W. B., Lakes, R. S. (1994) Size Effects Due to Cosserat Elasticity and Surface Damage in Closed-Cell Polymethacrylimide Foam. Journal of Materials Science, 29 (24), str. 6413–6419.

[17] Grbac, L. (2023) Finite Elements for Linear Analysis of Micropolar Continuum and Relationship between Linked Interpolation and Interpolations on Lie Groups in Linear Form. Doktorski rad, Sveučilište u Rijeci.

[18] Zienkiewicz, O. C., Taylor, R. L., Fox, D. (2013) The Finite Element Method for Solid and Structural Mechanics: Seventh Edition. Amsterdam: Elsevier.

[19] Taylor, R. L., Govindjee, S. (2020) FEAP: A Finite Element Analysis Program, Theory Manual.

[20] Providas, E., Kattis, M. A. (2002) Finite Element Method in Plane Cosserat Elasticity. Computers and Structures, 80 (27–30), str. 2059–2069.

[21] Grbčić, S., Jelenić, G., Ribarić, D. (2019) Quadrilateral 2D Linked-Interpolation Finite Elements for Micropolar Continuum. Acta Mechanica Sinica, 35 (5), str. 1001–1020.

[22] Kohansal-Vajargah, M., i drugi (2021) Vibration Analysis of Two-Dimensional Structures Using Micropolar Elements. Appl. Math. Mech., 42 (7), str. 999–1012.